🔓 **Open Access**
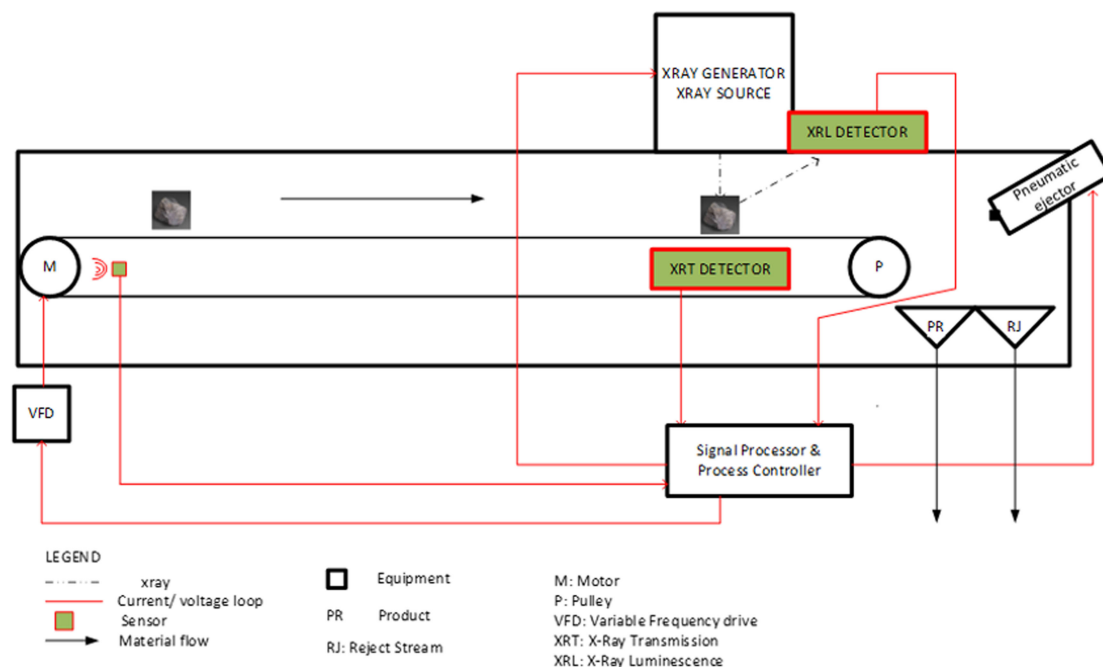
The New Paradox of Dual Modality X-Ray Diamond Sorting

Ernest Gomolemo Modise, *Member, IEEE*
Adamu Murtala Zungeru, *Senior Member, IEEE*
Joseph M Chuma, *Member, IEEE*
S.R.S. Prabaharan, *Member, IEEE*
Bokani Mtengi, *Member, IEEE*
Albert Ude
Zhivko Nedev

photonics SOCIETY

◆IEEE

The New Paradox of Dual Modality X-Ray Diamond Sorting

Ernest Gomolemo Modise,[1] **Member, IEEE,**
Adamu Murtala Zungeru (ORCID)**,**[1] **Senior Member, IEEE,**
Joseph M Chuma,[1] **Member, IEEE,**
S.R.S. Prabaharan,[4] **Member, IEEE, Bokani Mtengi,**[1] **Member, IEEE,**
Albert Ude,[2] **and Zhivko Nedev**[3]

[1]Department of Electrical, Computer and Telecommunications Engineering, Botswana International University of Science and Technology, Palapye, Botswana
[2]Department of Mechanical, Energy, and Industrial Engineering, Botswana International University of Science and Technology, Palapye, Botswana
[3]Department of Computer Science and Information Systems, Botswana International University of Science and Technology, Palapye, Botswana
[4]Directorate of Research, SRM Institute of Science and Technology, Potheri, Kattankulathur, Chengalpattu District, Tamil Nadu 603203, India

Abstract: Modern-day diamond sorting is achieved through the application of X-ray luminescence (XRL) and X-ray transmission (XRT) techniques. Sorting with XRL is limited to the class range of 1.25 mm to 32 mm because of self-absorption associated with larger diamonds, greater than 32mm. The effect of self-absorption is also a high-energy phenomenon in XRL. XRT is limited to sorting large size diamonds as the technique suffers poor contrast for diamonds smaller than 10mm. XRT measurements are immune to self-absorption for all sample sizes, while XRL measurements have good contrast for particles smaller than 32mm. The applications of these techniques have hitherto been used independently of each other and have subsequently progressed mutually exclusively. Here we analytically show a new paradox of a dual-modality X-ray diamond sorting combining XRL and XRT techniques' strengths. Key features of our new paradoxical model performance are contrast mitigation for small particles and self-absorption rejection for a large particle at high energy as well as improved particle detectability and classification.

Index Terms: Luminescence, fluorescence, transmission, self-absorption, contrast, detectability.

1. Introduction

Sensor-based sorting is a common technique of discriminating and separating materials, leveraging the constituent material's different physical properties. In X-ray sorting, the parameter of interest is absorption coefficient, which can be measured in luminescence or transmission configurations. In the context of diamond sorting, conventional sorting methods such as dense medium classification are capital and operational cost-intensive and sometimes causing operations to operate below optimal. Mineral exploration and winning have been with mankind since the dawn of time, and

the discovery of good ore grades seems to happen rapidly, leading to depletion [1]. Compounding these pressures introduces synthetic diamonds proving to be a real threat even for high-profit margin business as they are produced at significant quality, throughput, and competitive prices. MarketWatch.com published articles where they indicate that the synthetics industry's growth rate is exponential, with a projection of 7.85% of the diamond market being synthetics in the period 2019–2024 [2]. These business stresses pose a threat of closure, loss of investments, and general jobs [3]. A new paradigm to mining and mineral winning that will ensure that diamond operations remain competitive is the application of sensor-based sorting using X-ray technology. Current implementations of X-ray sensor-based sorting are primarily X-ray transmission and X-ray luminescence-based but not both. These techniques have developed in parallel and mutually exclusive. Object classification using X-ray is a function of material absorption rate and physical dimensions of the material. In that respect, the XRT sorting method suffers contrast for particles less than 10 mm [4], while the XRL suffers self-absorption for particles greater than 32mm, and for applications at high energy [5]. This places a limitation on the kind of application domain each technique can be used for.

The two sorting implementations face mutually exclusive sets of challenges [6]. To date, X-ray sensor-based diamond sorting methods employ either XRL or XRT in classification [7]. While these two methods rely on the measurement of the absorption coefficient of materials, there is no implementation in diamond sorting that uses both techniques jointly. Our task is to mathematically model the two-domain application to understand a suitable combining method that will allow us to gain from the advantage of each. Our approach focuses on contrast improvement and self-absorption rejection and simulates results from our combined sorting scheme. To the best of our knowledge, no model or implementation has been done in the context of a dual-modality diamond sorting scheme of both transmission and luminescence. We, therefore, carefully and holistically analyze the mathematical problems of transmission and luminescence and develop a new technique of joining the signals of interest. Our simulation is carried using absorption coefficient at a single energy level (monochromatic) and in polychromatic, where the absorption coefficient is a function of energy. The simulation utilized the 1keV – 20 MeV NIST published energy-dependent absorption coefficient data for different periodic table elements [7]. In the application of airport contraband search, it has been noted that X-ray transmission is sensitive to contrast at a small particle size range [8] while X-ray luminescence is immune to contrast for virtually all particle size ranges [8]. On the other hand, X-ray luminescence is adversely affected by self-absorption for large particle size ranges [8]. Self-absorption also manifests itself in luminescence when particles are irradiated with highly energetic X-rays [9]–[12]. In the transmission mode, the thin sample case presents a problem in which the input and output current intensities are essentially the same [13]. This scenario, in which the sample is not able to "carbon copy" itself through the penetrating X-rays, leaves one in the case of poor contrast [14]. The signal arrives at the detector in almost its complete entirety with very minimal information about the sample which it just traversed [15]. On the other hand, when the sample is of considerable thickness, the penetrating X-ray can embed on themselves significant information about the sample that it just traversed. This allows one to confidently detect and recover diamonds in size range greater than 10 mm [16]. There is a challenge of self-absorption in luminescence mode, which occurs due to X-rays traversing a significantly large sample or firing the sample with highly energetic X-ray energy [17]. This deficiency in X-ray luminescence has its application for large diamond recovery unattractive. Others [18] proposes a method that relies on the geometric setup of source, target, and sensor to mitigate the energy dependence on X-ray absorption.

In the present contribution, we advance a method that leverages each model's strength, jointly in monochromatic and polychromatic settings. We first analytically model X-Ray luminescence and X-Ray transmission for all the domains of interest to understand each model's behaviors in those sub-bands. In the end, we show a combined analytical model based on the tenets of XRL and XRT to leverage the strength of each technique. Key features of our combined analytical model performance are contrast mitigation for small particles and self-absorption rejection for a large particle at high energy as well as improved particle detectability and classification.
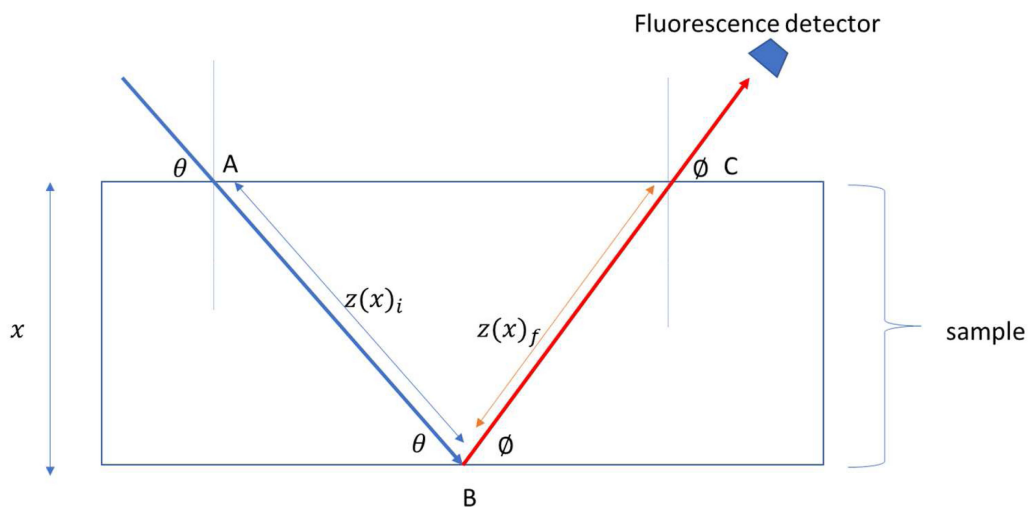
Fig. 1. X-ray Fluorescence.

The rest of this paper is organized as follows: Section 2 highlights the background and motivation for the use of X-rays in diamond sorting. In Section 3 is the problem definition. In Section 4, the Inversion Methods is discussed, including the monochromatic sorting modes and their joint approach are presented and the polychromatic sorting mode, by first identifying the high energy self-absorption dependence of luminescence mode, followed by the analysis of transmission signal at high energy. We then combine the signals of interest and show signal variation preservation at high energies. Section 5 highlights a joint detection improvement, and conclusions are finally drawn in Section 6.

2. Background And Motivation

X-ray fluorescence/luminescence and transmission classification methods are a class of inverse problems that are based on the difference in material X-ray attenuation rates, known as absorption coefficient. Beer's Law compactly describes the two processes:

$$I = I_o e^{-\mu(E)t} \tag{1}$$

Where I is the intensity of radiation at the detector, Io is the intensity of the incident radiation, E is the photoelectrons' energy, and t is the sample or analyte thickness. The subtle difference comes from the fact that luminescence is a two-step process, while transmission can be thought of as a single-step process. Fig. 1 is a geometrical representation of the fluorescence process. An X-ray is an incident on a sample of thickness x at an angle θ. If the incoming X-ray has sufficient energy, it causes an inner bound state electron to be ejected, leaving a core hole, which in turn gets filled by an outer valence electron dropping from a higher shell to the core hole. During this process, an X-ray quantum equivalent to the bandgap will be emitted. The emission of such a secondary X-ray is scattered equally in all directions. In this example, an energy dispersive sensor is placed at angle ϕ above the sample. The variation of intensity through the absorption media as a function of thickness is given by;

$$dI = -\mu(E) I_o e^{-\mu(E)z_i(x)} dx. \tag{2}$$

Where x is the distance traversed by X-rays through the sample thickness and $z(x)$ is the distance travelled by the X-rays in the sample, which in Fig. 1 is $z(x)_i$ and $z(x)_f$ respectively.

Using Eqn. (1), and redefining $z(x)_i$ and $z(x)_f$ parametrically in x,

$$z(x)_i = \frac{x}{\sin\theta} \text{ and } z(x)_f = \frac{x}{\sin\varnothing} \tag{3}$$

Accounting for the incident path length (blue), the intensity

$$dI_i = -\mu(E)\,I_o e^{-\mu(E)z(x)_i}dx = -\mu(E)\,I_o e^{-\mu(E)\frac{x}{\sin\theta}}dx \tag{4}$$

And for the fluorescence path length (red), the intensity at the detector is given by,

$$dI_f = dI_i e^{-\mu(E)\frac{x}{\sin\varnothing}}dx \tag{5}$$

$$dI_f = \left(-\mu(E)\,I_o e^{-\mu(E)\frac{x}{\sin\theta}}\right)e^{-\mu(E_f)\frac{x}{\sin\varnothing}}dx \tag{6}$$

$$dI_f = \left(-\mu(E)\,I_o e^{-\mu(E)\frac{x}{\sin\theta}}\right)e^{-\mu(E_f)\frac{x}{\sin\varnothing}}dx = -\mu(E)\,I_o e^{-\left(\frac{\mu(E)}{\sin\theta}+\frac{\mu(E_f)}{\sin\varnothing}\right)x}dx \tag{7}$$

And

$$I_f \propto \int_0^t -\mu(E)\,I_o e^{-\left(\frac{\mu(E)}{\sin\theta}+\frac{\mu(E_f)}{\sin\varnothing}\right)x}dx \tag{8}$$

While the proportionality takes note of the fact that other aspects such as the detector geometry are not accounted for in the derivation.

$$I_f \propto \frac{\mu(E)\,I_o\left[1 - e^{-\left(\frac{\mu_t(E)}{\sin\theta}+\frac{\mu_t(E_f)}{\sin\varnothing}\right)t}\right]}{\frac{\mu_t(E)}{\sin\theta}+\frac{\mu_t(E_f)}{\sin\varnothing}} \tag{9}$$

Including the detector solid angle and efficiency

$$I_f = \frac{\varepsilon\Delta\Omega\mu(E)\,I_o\left[1 - e^{-\left(\frac{\mu_t(E)}{\sin\theta}+\frac{\mu_t(E_f)}{\sin\varnothing}\right)t}\right]}{4\pi\frac{\mu_t(E)}{\sin\theta}+\frac{\mu_t(E_f)}{\sin\varnothing}} \tag{10}$$

Based on the same approach, the intensity of X-rays at the transmission detector is given by,

$$I = I_o e^{-\mu_t(E)t} \tag{11}$$

In this mode, the X-rays traverse the sample perpendicular to the plane cutting horizontally through the sample, and as such, there is only one path to be considered, Fig. 2.

2.1 Application of X-Ray Luminescence Sorting

The X-Ray Luminescence working principle can thus be exploited to determine the elemental composition of various materials. The fluoresced X-ray intensity as a function of the absorption coefficient is given by:

$$I_f = I_o\frac{\varepsilon\Delta\Omega\mu_\chi(E)}{4\pi}\frac{\left\{1 - e^{-\left(\frac{\mu_{tot}(E)}{\sin\theta}+\frac{\mu_{tot}(E_f)}{\sin\phi}\right)t}\right\}}{\frac{\mu_{tot}(E)}{\sin\theta}+\frac{\mu_{tot}(E_f)}{\sin\phi}} \tag{12}$$

Where ϵ is the fluorescence efficiency, $\Delta\Omega$ is the solid detector angle, E_f is the energy of the fluoresced X-ray, θ is the incident angle between the sample and the X-ray, ϕ is the exit angle between the sample and the fluoresced X-ray, $\mu_\chi(E)$ is the absorption coefficient of the element of interest and $\mu_{tot}(E)$ is the total absorption of the sample.

Incident x-ray
I_0

t

sample

$I_0 e^{-\mu(E)t}$
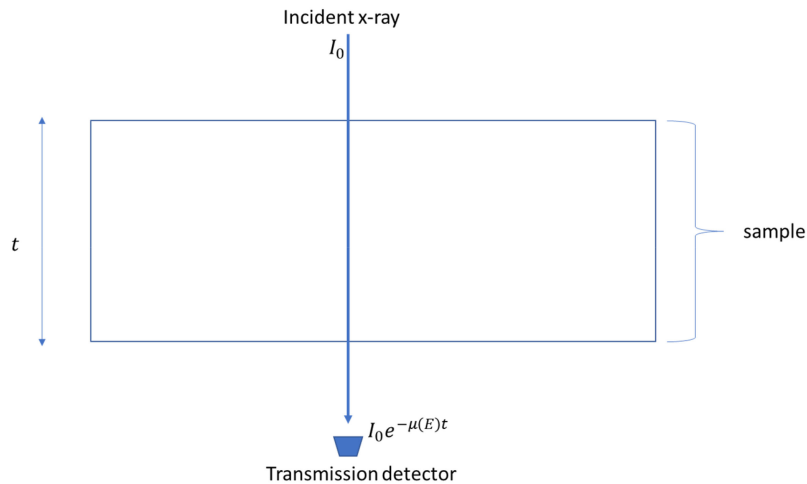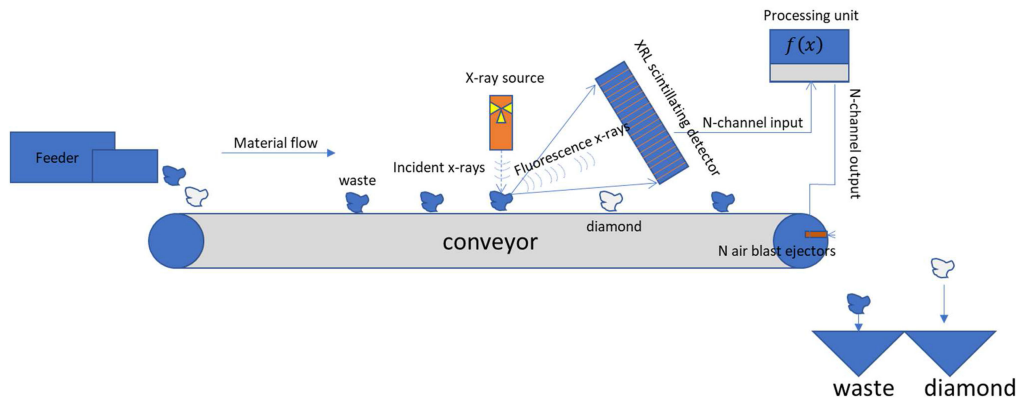
Transmission detector

Fig. 2. X-ray Transmission.

Fig. 3. Application of X-ray Luminescence.

Fig. 3 shows the cross-sectional arrangement of the inside of an X-ray luminescence machine. The system consists of a vibrating feeder, an internal machine belt, an X-ray tube, a photomultiplier tube, an n-channel detector, an n-channel pneumatic ejector module, etc a signal processing unit.

Primary X-rays are generated by the X-ray generator or tube and are directed on the material. The incident X-ray excites the material and causes it to emit radiation. The emitted radiation is captured by a detector and compared with a threshold for classification.

2.2 Application of X-Ray Transmission Sorting

The intensity of X-ray radiation transmitted through a sample is defined by Beer's Law. This process is a single path process in which the X-rays source, the sample, and the sensor are placed perpendicular in a collinear path, Fig. 4. The strength of transmitted intensity through a sample of thickness t due to an incident X-ray radiation of intensity I_o, is given by the Eqn. (13) as:

$$I = I_0 e^{-\mu t} \tag{13}$$

Where I_O, and I, are the incident X-ray intensity and transmitted X-ray intensity, respectively, and μ is the absorption coefficient.

The system consists of an electrically powered radiation source with energy in the order of tens of keV placed on top of a conveying system. The radiation penetrates the particles; some of the
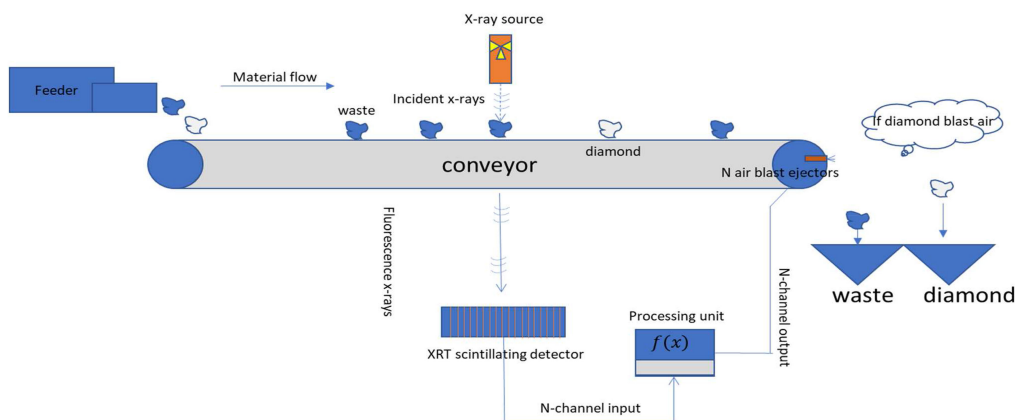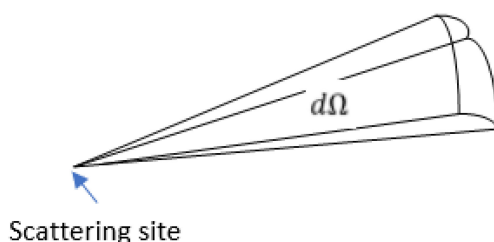
Fig. 4. Application of X-ray Transmission.

Fig. 5. Solid angle $d\Omega$.

radiation is absorbed while the residual radiation is recorded by the detector. The sensor consists of scintillating crystals that measure radiation intensity as of the counts intensity of the transmitted X-ray. The X-rays are transmitted through the sample with varying intensity as per Eqn. 13.

2.3 Details of Absorption Coefficient $\mu(E)$

While equations (10) and (11) of luminescence and transmission are functions of the absorption coefficient, $\mu(E)$, these equations provide an average behavior of material absorption of X-rays as a function of energy. A lot more elemental information is encapsulated in $\mu(E)$, which is unpacked by considering the relationship between the absorption coefficient and scattering cross-section $\sigma(E)$.

$$\mu(E) \propto \sigma(E) \tag{14}$$

Measurement of the absorption coefficient is closely related to an analysis of scattering cross-section, σ [19]. The scattering cross-section is defined as the ratio of the flux of photoelectrons leaving the area subtended by solid angle $d\Omega$ per unit time to the flux of incident photoelectrons, Fig. 5.

The flux of incident photoelectrons per unit time J is given by:

$$J_o = n\frac{\bar{h}}{m} Im\left(\psi_0{}^* \nabla \psi_0\right) \tag{15}$$

While the flux due to the scattered wave function across a surface dS subtended by the solid angle $d\Omega$ is

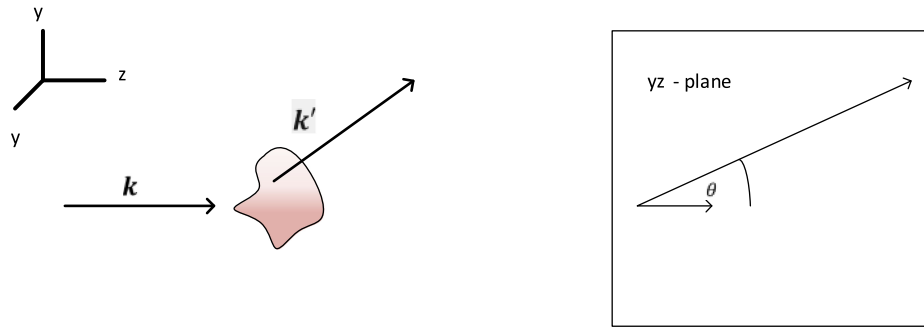$$J_s = n\frac{\bar{h}}{m} Im\left(\psi_s{}^* \nabla \psi_s\right) dS \tag{16}$$

Fig. 6. Scattering Phenomena.

Therefore, the differential cross-section is:

$$d\sigma = \frac{J_s}{J_o} = \frac{n\frac{\bar{h}}{m} Im\left(\psi_s^*\nabla\psi_s\right)dS}{n\frac{\bar{h}}{m} Im\left(\psi_0^*\nabla\psi_0\right)} = \frac{Im\left(\psi_s^*\nabla\psi_s\right)dS}{Im\left(\psi_0^*\nabla\psi_0\right)} \tag{17}$$

Since the form ψ_0 is known, our next objective is to find ψ_s. To do so, we need to find a suitable means of describing the system. Consider the system as in Fig. 4, in which an energetic beam of X-rays is incident on an atomic potential, which leads to a scattering phenomenon.

By assuming the direction of the incident photoelectrons to be along the z-axis, the incident photoelectrons can be characterized by a wavefunction $\psi_0(\overline{r})$ and a wavevector k, then,

$$\psi_0(\overline{r}) = exp\left(ikz\right) \tag{18}$$

The photoelectron is incident on an atomic potential or scattering potential $V(\overline{r})$. Subsequently, the photoelectrons are scattered in a direction characterized by a wavevector k', such that the total wavefunction ψ after a scattering event is composed of the incident wavefunction plus the scattered wavefunction.

$$\psi\left(r\right) = \psi_0(\overline{r}) + \psi_s(\overline{r}) \tag{19}$$

The total Hamiltonian H of the system is given by:

$$H = -\frac{\bar{h}^2}{2m}\nabla^2 + V\left(\bar{r}\right) \tag{20}$$

And Schrodinger's equation for the scattering problem is:

$$H\psi = E\psi \tag{21}$$

Where

$$E = \frac{\bar{h}^2 k^2}{2m} \tag{22}$$

Combining (21) and (22) yields

$$\left(-\frac{\bar{h}^2}{2m}\nabla^2 + V\left(\bar{r}\right)\right)\psi = \frac{\bar{h}^2 k^2}{2m}\psi \tag{23}$$

Rearranging (23) we obtain,

$$\left(\nabla^2 + k^2\right)\psi\left(r\right) = \frac{2m}{\bar{h}^2}\psi\left(r\right)V\left(r\right) \tag{24}$$

The information of atomic field $V(r)$ responsible for the scattering phenomena is captured in Eqn. (24). It is impossible to measure $V(r)$ directly, but by measuring its effects on $\psi(r)$ we can decipher information about the atomic site.

Eqn. (12) is a Helmholtz equation with a solution that leads to:

$$\mu(E) = \mu(k) \propto \sigma(k) = \sum_i \int \frac{C_l^2}{2k^2 r^2} (1 + \sin(2kr + 2\gamma_l)) P_l^2(\cos\theta) \, d\Omega \tag{25}$$

Where $P_l(\cos\theta)$ is a solution to a homogeneous Legendre differential equation that come about as a result of applying far-field boundary condition to Eqn. (24), i.e., where $V(r) = 0$. Another yet important but undisclosed condition that simplifies the solution of Eqn. (24) is the highly energetic plane wave approximation assumption. This assumption is valid by virtue of the comparison between atomic scale and detector size, distance to a detector, and photoelectrons' working energy.

The result of the integral of (25) can be written as:

$$\mu_1(k) = \mu_{o1}(1 + X_{o1}(k)) \tag{26}$$

Where $X_{o1}(k)$, is the sinusoidal variation of the absorption coefficient for single elastic scattering. By incorporating the fact that the scattering is not elastic and accounting for the nearest neighbour atoms, the total sinusoidal component of the absorption coefficient is:

$$X(k) = \sum_j \frac{N_j e^{-2k^2 \sigma_j^2} e^{-R_j/\lambda(k)} f_j(k)}{k R_j^2} \sin(2kR_j + \delta_j(k)) \tag{27}$$

Where N_j is the coordination number of the jth atomic species, σ_j^2 is the Debye-Waller factor and $\lambda_j(k)$ is, $f_j(k)$ and $\delta_j(k)$, are the scattering phase and amplitude of the neighbouring atom, respectively. This is the extended X-ray absorption fine structure (EXAFS) for the expression of (27), useful in our polychromatic diamond sorting.

In retrospect of the above, the detailed absorption coefficient $\mu(E)$ is given by:

$$\mu(E) = \mu(k) = \bar{\mu}(k) \left(1 + \sum_j \frac{N_j e^{-2k^2 \sigma_j^2} e^{-R_j/\lambda(k)} f_j(k)}{k R_j^2} \sin(2kR_j + \delta_j(k))\right) \tag{28}$$

Where the transformation between the incident X-ray energy E and wave vector k is given by;

$$k = \sqrt{\frac{2m}{\hbar}(E - E_o)} \tag{29}$$

Where E_o is the energy estimated for the near edge jump.

3. Problem Definition

The task of sorting involves discriminating material by their unique properties. Kimberlite is the parent material hosting diamonds [20]. In the host material, a diamond can exist in the locked up state or free state. When diamonds are fully encapsulated within the parent rock, they are said to be locked up [21]. Freeing up diamonds from a locked-up state to a free state is achieved through a comminution process called liberation [22]. In today's diamond processing plants, the succeeding stage after liberation is dense media separation and sensor-based sorting based on X-ray luminescence or X-ray transmission sorting. X-ray sensor-based sorting rely on the measurement of material absorption coefficient $\mu(k)$ or its sinusoidal component $X(k)$. In general, diamondiferous kimberlites are characterized by the presence of other associated compounds including ilmenite $FeTiO_3$, garnet $A_3B_2Si_3O_{12}$, where A is a divalent cation (Fe^{2+}, Ca^{2+}, Mg^{2+}, Mn^{2+}) and B is a trivalent cation (Fe^{3+}, Al^{3+}, Cr^{3+}) and phlogopite $KMg_3AlSi_3O_{10}(F, OH)_2$. Diamond has a chemical formula, C (isometric, a face-centered cubic arrangement in it) exhibiting sp3 hybridization. Thus, the task of sorting for diamonds is separating diamonds from ilmenite, garnets, and phlogopite. Interestingly, these compounds have a similar density as diamonds such that in the dense media separation, these materials are classified together with diamonds as the Dense Media Separation (DMS) the cut-off point is generally around 2.65 kg/m3 [22]. DMS cut-off removes most of the gangue material below the density of 2.65 to tailings (waste). However, a lot

more material is classified together with diamonds, leaving a massive task of sorting, which still requires an automated sorting of some kind [23]. While one can use the DMS to reduce the sorting task, there is a limitation as to the size of the particle that can be passed through a DMS circuit [24]. Additionally, the operational cost of a DMS circuit is exacerbated by the need for high volumes of water, increasing need for slime disposal dams, environmental pollution and legal compliance matters, and the cost of pump component replacements due to high wear associated with the transport of multiphase fluids containing gravel [25].

In this respect, it becomes now sensible for diamond-producing companies to tackle the sorting of what would otherwise be DMS input material and other larger size particle material through XRL and XRT sensor-based sorting. Knowledge of the compounds present in the kimberlite and their absorption coefficient becomes an obvious step in implementing sensor-based sorting based on luminescence or transmission. Kleimann *et al.* [26], describe the absorption coefficient of all elements in the periodic table. Through understanding the molecular composition of the material, one can calculate the absorption coefficient of the common compounds found in kimberlite, including diamond with (30)

$$\mu_{com} = \sum_e W_e \mu_e \qquad (30)$$

Where μ_{com} is the weighted sum of the absorption coefficient of the elements making up the compound, where μ_e and W_e, are the element absorption coefficient and its corresponding proportion in the sample.

Besides, the compound or mixture consists of diamond, ilmenite, phlogopite, and garnets in proportions $\{W_c, W_i, W_p, W_g\}$ and absorption coefficients $\{\mu_c, \mu_i, \mu_p, \mu_g\}$. The sample absorption coefficient can be described using (31) as

$$\mu_{com} = W_c\mu_c + W_i\mu_i + W_p\mu_p + W_g\mu_g \qquad (31)$$

or

$$\mu_{com} = W_c\mu_c + \left(W_i\mu_i + W_p\mu_p + W_g\mu_g\right) \qquad (32)$$

Where

$$\left(W_i\mu_i + W_p\mu_p + W_g\mu_g\right) = \mu_{other} \qquad (33)$$

And

$$W_c\mu_c = \mu_{target} \qquad (34)$$

And

$$\mu_{total} = \mu_{com} = \mu_{target} + \mu_{other} \qquad (35)$$

When $\mu_{other} = 0$, and $\mu_{total} = \mu_{target}$, the sample is referred to as a pure sample [29], and in our case, represents a freed-up diamond. If $\mu_{target} < \mu_{other}$, the sample is referred to as a dilute sample and $\mu_{target} > \mu_{other}$ is referred to as a concentrated sample. Fig. 7 shows the absorption coefficients of carbon and common compounds/mixtures (ilmenite, phlogopite, garnet) generally found with kimberlite in the energy range 1 keV – 20 MeV. The graph shows that carbon, ilmenite, and phlogopite have very different absorption coefficient in the region 6 keV – 80 keV. This is of profound interest as it forms the basis for diamond sorting in both XRL and XRT.

4. Inversion Methods

Measurement of $\mu(k)$ or $X(k)$ can be done in luminescence or transmission. In luminescence, the emitted X-ray intensity from a sample is presented in (10). In the transmission mode, the intensity of X-rays transmitted through the sample is as presented in (11). On the other hand, the transmission mode has been shown to perform best for large or concentrated samples while it experiences poor contrast for thin and dilutes samples [29]. In general, either luminescence or transmission
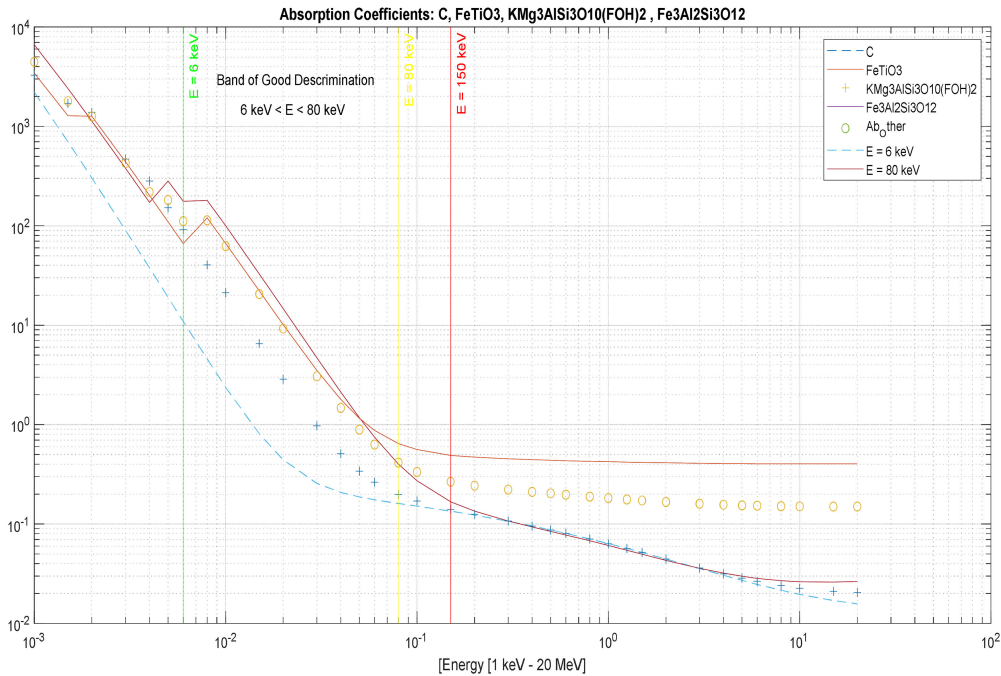
Fig. 7. Absorption Coefficient of Carbon, Ilmenite, Garnet, and Phlogopite.

modes can be operated at a single X-ray wavelength or different wavelengths [30]. Hence our mathematical simulations mimic these setups. The analysis in which an absorption coefficient is at a single wavelength is referred to as monochromatic, while that for which different energies levels are used is called polychromatic mode.

4.1 Monochromatic Sorting Mode – Varying Sample Length

4.1.1 XRL Analytical Model: In a monochromatic simulation mode, our analysis investigates luminescence intensity as a function of sample thickness, while the firing energy is maintained constant. The variation of luminescence intensity with thickness is characterized by the gradient.

$$\frac{dI_f}{dt} = \frac{I_0 \varepsilon \Delta \Omega \mu_\chi (E)}{4\pi} e^{-\left[\frac{\mu_{tot}(E)}{\sin \theta} + \frac{\mu_{tot}(E_f)}{\sin \phi}\right]t}, \tag{36}$$

which has a first-order Taylor series expansion of

$$\frac{dI_f}{dt} \approx \frac{I_0 \varepsilon \Delta \Omega \mu_\chi (E)}{4\pi} \left(1 - \left[\frac{\mu_{tot}(E)}{\sin \theta} + \frac{\mu_{tot}(E_f)}{\sin \phi}\right]t\right) \tag{37}$$

Since E is a constant, it implies that $\mu_{tot}(E)$ and $\mu_{tot}(E_f)$ are also constants.

Fig. 8 is a measurement of luminescence intensity for different materials and shows a negative slope for each type of material found in kimberlite. It shows a degradation in classification as material thickness increases which is consistent with the work of [8]. For a thin sample, the Taylor series expansion of (36) is

$$\frac{dI_f}{dt} = \frac{I_0 \varepsilon \Delta \Omega \mu_\chi (E)}{4\pi}; \tag{38}$$

Which is a function of $\mu_\chi(E)$ only. Interestingly, this result states that no two lines of intensity of different materials will cross each other in this region. This result is also consistent with Fig. 9, which are graphs of material luminous intensity for particles below 20 mm.
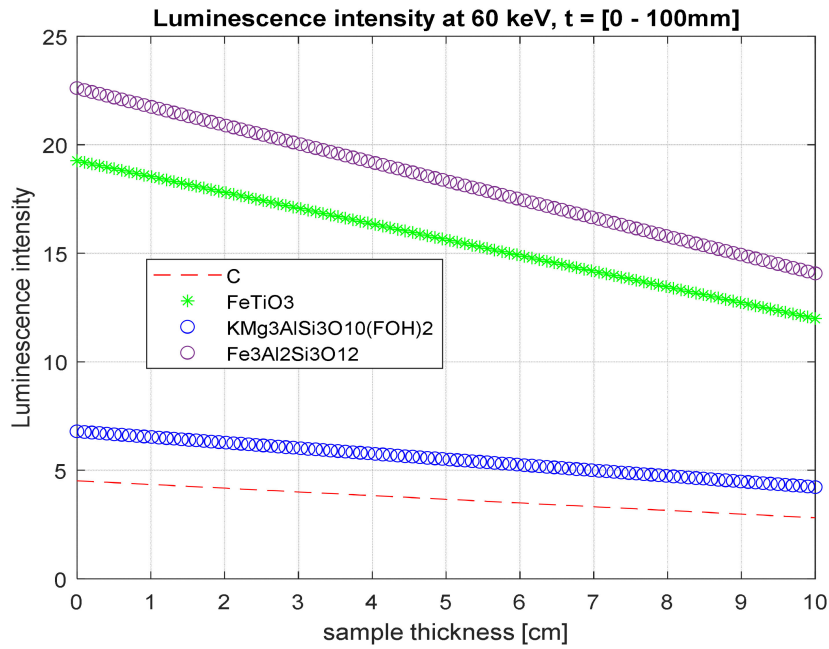
Luminescence intensity at 60 keV, t = [0 - 100mm]

Fig. 8. Measurement of Luminescence Intensity.

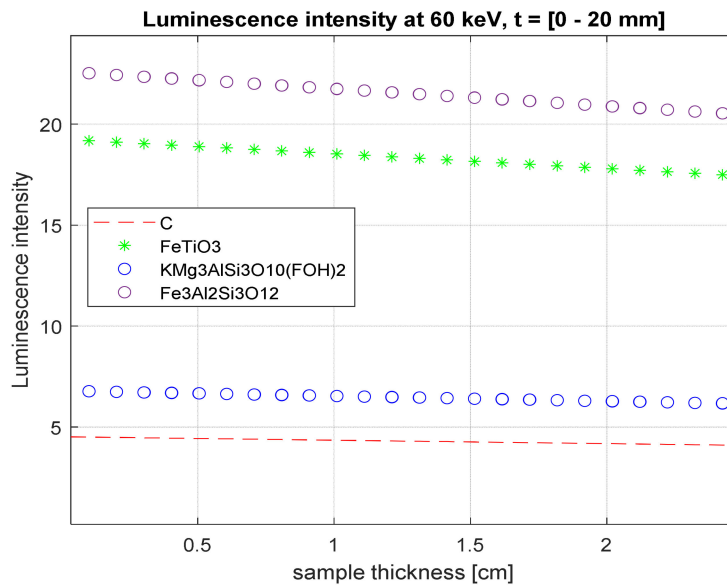**Luminescence intensity at 60 keV, t = [0 - 20 mm]**

Fig. 9. Zoomed Luminescence Intensity between [0–20mm].

The condition for what is considered a thin sample is,

$$\left[\frac{\mu_{tot}(E)}{\sin\theta} + \frac{\mu_{tot}(E_f)}{\sin\phi} \right] t \leq 0.404 \qquad (39)$$

Our objective is to detect and classify rock with at least 70% diamond and 30% other material. For $E = 60$ keV, $\theta = \frac{\pi}{2}$, $\phi = \frac{\pi}{12}$, $E_f = 60$ keV, Resulting in $t \leq 1.205$ mm for the category of thin samples.

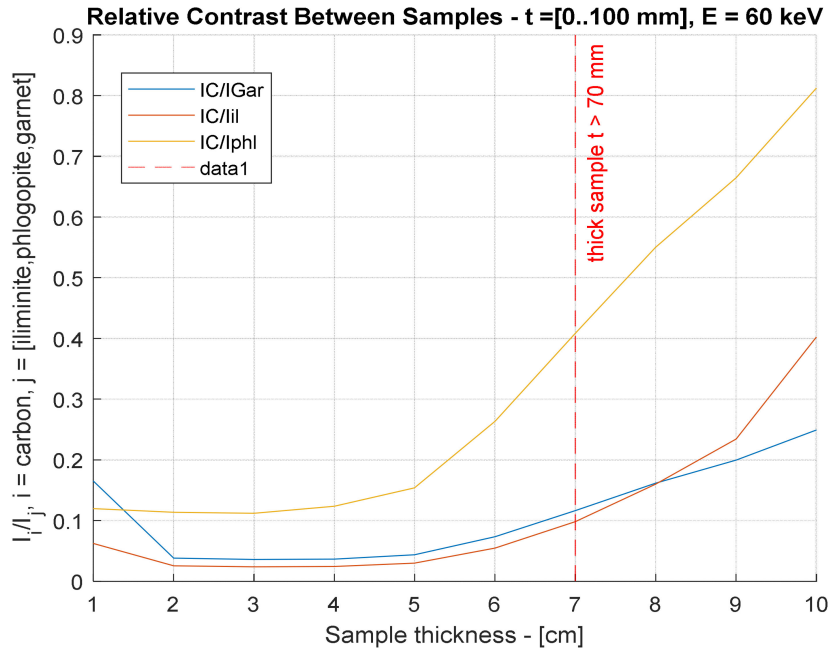**Relative Contrast Between Samples - t =[0..100 mm], E = 60 keV**

Fig. 10. Inter-Contrast I_i/I_j Between Material *i* and *j*.

Generally, diamonds of this size are considered uneconomic to recover. The other extreme is the large sample case, for which the exponent vanishes. This occurs when

$$\left[\frac{\mu_{tot}(E)}{\sin\theta} + \frac{\mu_{tot}(E_f)}{\sin\phi}\right] t \geq 2.929 \qquad (40)$$

Such that $t \geq 8.730$ mm

Revisiting the large sample simplification, it is evident that $I_f \propto \mu_\chi(E)$, is a constant line with respect to thickness, and again, is a useful feature for sorting. The choice of operating X-ray energy plays a significant role in the optimization of self-absorption phenomena [41]. Fig. 10 shows that the XRL sorting method is not affected by contrast for a good range of particle size. Recalling a ratio of unity indicates poor inter-signal contrast, while a ratio significantly lower than 1, typically below 30% shows good inter-signal contrast. Similarly, the convergence of the signals at high thickness material, testifies the impact of self-absorption for large particle sizes.

4.1.2 Dealing With Self Absorption: In order to address the challenge of self-absorption primarily for relatively thick concentrated samples, samples with $\mu_\chi \sim \mu_t$, fired at high X-ray energy, a numerical model of self-absorption is compiled to give some insight to the type of closed analytical model to incorporate when dealing with this phenomenon. It is imperative to determine the energy threshold that will ensure self-absorption is minimized. For this, we need to deviate slightly from a monochromatic setting to allow for a derivation of an energy-dependent self-absorption model.

For thick, concentrated samples such that $\mu_\chi \sim \mu_{other}$ and $\mu_\chi \sim \mu_{tot}$,

$$I_f = \frac{I_o\,\varepsilon\Delta\Omega}{4\pi}\frac{\mu_\chi(E)}{\frac{\mu_{tot}(E)}{\sin\theta} + \frac{\mu_{tot}(E_f)}{\sin\phi}} \qquad (41)$$

It cannot be simplified further and remains a function of energy *E*. Thus (41) can be re-casted as;

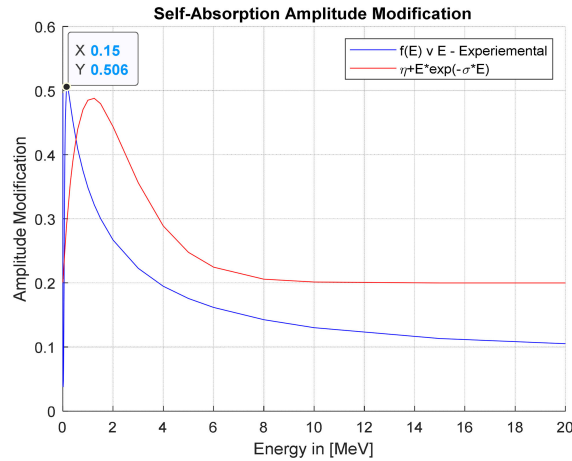$$I_f = \frac{I_o\,\varepsilon\Delta\Omega}{4\pi}f(E) \qquad (42)$$

Fig. 11. Numerical Self-Absorption Factor and Analytical Self-Absorption Factor.
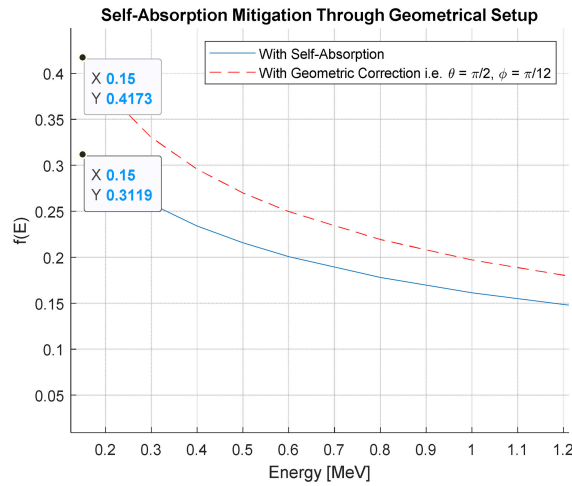

Fig. 12. Self-Absorption mitigation through the source-detector geometric setup.

Where

$$f(E) = \frac{\mu_\chi(E)}{\frac{\mu_{tot}(E)}{sin\theta} + \frac{\mu_{tot}(E_f)}{sin\phi}} \tag{43}$$

One way to minimize self-absorption for a thick sample is to obtain the value of $f(E)$ such that self-absorption can be reduced [42], and this is similar to:

$$\max(I_f) = \frac{I_o\,\varepsilon\Delta\Omega}{4\pi} * \max(f(E)) \tag{44}$$

A plot of $f(E)$ for thick samples, Fig. 11 ($f(E)$ vs E) indicates that in the case of diamonds, the optimal operating point to minimize self-absorption of thick sample is at 150 keV.

Unfortunately, in the region $\geq 150\ keV$, the materials to be sorted whose absorption coefficients are not very distinct from each other, Fig. 7, and further this determination will only be useful for monochromatic setting sorter operation as E_{max}, is a single point in the entire range. A simulation of $f(E)$ allows us to derive an approximate attenuation factor for XRL- EXAFS signal at high energies. This led to following functional form of the self-absorption effect for polychromatic operation.
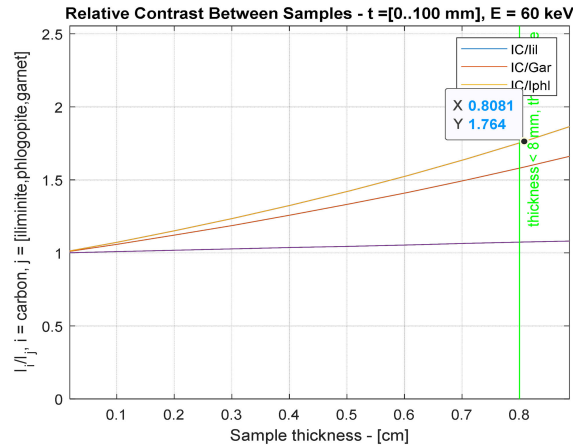
$$f(E) = Ee^{-\gamma E} \tag{45}$$

Fig. 13. Poor inter-material contrast I_i/I_j below 8 mm.

4.1.3 Geometric Self-Absorption Mitigation: The function $f(E)$ can be made simpler by means of source-detector configuration [42]. Since $\mu_\chi \sim \mu_{other}$ and $\mu_\chi \sim \mu_{tot}$, one way to eliminate the energy dependence of the denominator is to place the source and detector such that:

$$\frac{\mu_{tot}(E)}{\sin\theta} '' \frac{\mu_{tot}(E_f)}{\sin\phi} \tag{46}$$

This condition can be achieved through a grazing exit configuration, such that the angle ϕ of the exiting luminescence signal is very small so that condition (21) is satisfied. By selecting the angle of incidence at 90°, $\frac{\pi}{2}$ and the angle of exit to be 15°, $\frac{\pi}{12}$, the effect of self-absorption can be mitigated [43]. Fig. 11 shows the result of this, showing signal recovery improvement because of geometric orientations of source and detector.

4.1.4 Xrt Analytical Model: The analytical model for X-ray intensity in transmission through a sample is given by:

$$I_T = I_o e^{-\mu t} \tag{47}$$

For a thin sample,

$$\frac{I_T}{I_o} = e^{-\mu t} \geq 0.9 \tag{48}$$

For X-ray energy of 60keV, this corresponds to $t \leq 10$ *mm*. Which is a linearly increasing function of thickness. Fig. 13 shows that for small particle size range, typically for thickness below 10 mm, the XRT performs poorly as it cannot contrast between samples.

For very large sample

$$\frac{I_T}{I_o} = e^{-\mu t} \leq 0.1 \tag{49}$$

For X-ray energy of 60keV, this corresponds to $t \geq 13.12$. A desirable contrast criterion is for I_j/I_i, to be significantly different from 1. Fig. 14 shows a contrast criterion based on the transmission of X-ray intensity relative to diamonds, making XRT a good model for sorting large diamonds material.

4.1.5 Combined Model In Monochromatic Source Mode: Here, we demonstrated the combined model in monochrome source mode. Note that (10) represents the luminescence signal for each element, compound, or mixture in the sample and (11) depicts the transmitted signal from each element, compound, or mixture. We know the values of the functions at the two extremes. However, a simpler model is not clear in the intermediate particle size range. From our knowledge that XRL suffers from self-absorption for a thick sample and at high energies but does not suffer from poor contrast at small particle size range, while XRT suffers poor contrast at a thin sample but does not
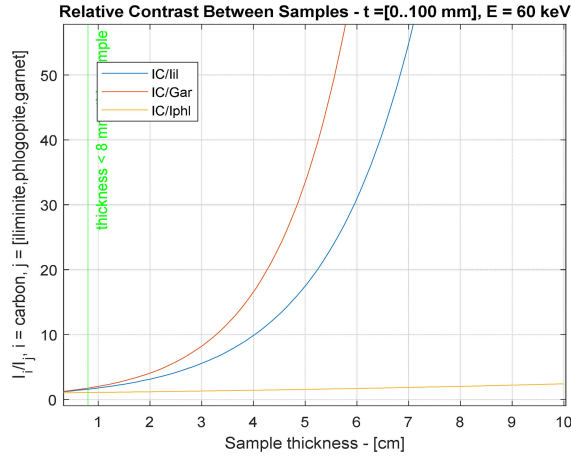
Fig 14. Good Inter-Material Contrast for Particles $>$ 10 starting around 20mm.

encounter self-absorption for large particles, a combination of the XRL and XRT signal is implored to leverage the benefits of each sorting method. The directed dual-mode XRL and XRT signal are then defined as:

$$I_{total} = \frac{I_o \varepsilon \Delta\Omega \mu_\chi\,(E)}{4\pi} \frac{\left\{1 - \left\{e^{-\left(\frac{\mu_{tot}(E)}{\sin\theta} + \frac{\mu_{tot}(E_f)}{\sin\phi}\right)t}\right\}\right\}}{\left[\frac{\mu_{tot}(E)}{\sin\theta} + \frac{\mu_{tot}(E_f)}{\sin\phi}\right]} + I_o e^{-\mu t} \tag{50}$$

In order to always ensure the distinction between target sample (diamond) and waste, we desire plots of the different signals to be parallel in all the regions of interest. A trivial case of this is:

$$\frac{dI_{tot}}{dt} = \frac{dI_T}{dt} + \frac{dI_f}{dt} = 0 \tag{51}$$

This will ensure that the obtained combined signals for the different materials are parallel to each other with zero gradients or the same gradient.

For thin samples in luminescence mode,

$$I_f = \frac{I_{of}\varepsilon\Delta\Omega\mu_\chi}{4\pi} \frac{\left\{1 - \left[1 - \frac{\mu_{tot}(E)}{\sin\theta} + \frac{\mu_{tot}(E_f)}{\sin\phi}\right]t\right\}}{\left[\frac{\mu_{tot}(E)}{\sin\theta} + \frac{\mu_{tot}(E_f)}{\sin\phi}\right]} \approx \frac{I_o \varepsilon \Delta\Omega \mu_\chi t}{4\pi} \tag{52}$$

For thin samples in the inverse transmission signal,

$$I_{oT} = I_T e^{\mu_\chi t} \approx I_T\left(1 + \mu_\chi t\right) \tag{53}$$

If we were to combine the two signals I_f and I_{oT} the result will be (39)

$$I_{tot} = \frac{I_{of}\varepsilon\Delta\Omega\mu_\chi t}{4\pi} + I_T\left(1 + \mu_\chi t\right) \tag{54}$$

$$\frac{dI_{tot}}{dt} = \frac{I_{of}\varepsilon\Delta\Omega}{4\pi}\mu_\chi + I_T\mu_\chi = \mu_\chi \sum_{i=1}^{2}\beta_i \tag{55}$$

Where the β_i are detector parameter or gains, with $i = 1$ implying strength of XRT signal and $i = 2$ is the strength of the XRL signal. Our design focuses on the $\beta_i's$ that equally enhances either signal mode. This can be achieved through hardware amplification or through algorithmic levelling of the two signals in the signal processing step. The significance of (54) is that, for a sample consisting

TABLE 1

Monochromatic Contrast Performance Pre-System Joining.

Contrast	XRT		XRL	
I_o/I_c (dB)	$< 10mm$	$> 32mm$	$< 10mm$	$> 32mm$
	0	6	3.54	2.81

Subscript *o* is for other material, while subscript *c* is for carbon or diamond.

pure carbon (diamond), pure iliminite, pure phlogopite, and pure garnets, the graphs I_{tot} are distinct due to the fact that each material has a unique μ_χ.

For thick samples we are using (10) and (11) to solve for μ_χ, we see that this is rather trivial for the XRT signal and

$$\mu_\chi t = \ln \frac{I_{oT}}{I_T} \tag{56}$$

However, to solve for μ_χ in the luminescence signal, (10) involves transcendental equations and application of Newton Raphson iteration procedure, but using dimensional analysis, one notices that the dimension of (57)

$$\frac{I_f}{I_{of}} = \frac{\varepsilon \Delta \Omega \mu_\chi}{4\pi} \frac{\left\{ 1 - e^{\left[\frac{\mu_{tot}(E)}{\sin\theta} + \frac{\mu_{tot}(E_f)}{\sin\phi} \right] t} \right\}}{\left[\frac{\mu_{tot}(E)}{\sin\theta} + \frac{\mu_{tot}(E_f)}{\sin\phi} \right]} \tag{57}$$

is the same as the dimension of $\mu_\chi t$ and hence we define a new quantity.

$$I_J = \frac{I_f}{I_{of}} + \ln \frac{I_{oT}}{I_T} = \frac{\varepsilon \Delta \Omega \mu_\chi (E)}{4\pi} \frac{\left\{ 1 - \left\{ e^{-\left(\frac{\mu_{tot}(E)}{\sin\theta} + \frac{\mu_{tot}(E_f)}{\sin\phi} \right) t} \right\} \right\}}{\left[\frac{\mu_{tot}(E)}{\sin\theta} + \frac{\mu_{tot}(E_f)}{\sin\phi} \right]} + \mu_\chi t \tag{58}$$

This simplification allows us to reject the geometric effects in the absorption coefficient in the denominator through a derivative of I_J with respect to thickness, (58).

$$\frac{dI_J}{dt} = \frac{\varepsilon \Delta \Omega \mu_\chi (E)}{4\pi} e^{-\left(\frac{\mu_{tot}(E)}{\sin\theta} + \frac{\mu_{tot}(E_f)}{\sin\phi} \right) t} + \mu_\chi (E) \tag{59}$$

For thick samples $[\frac{\mu_{tot}(E)}{\sin\theta} + \frac{\mu_{tot}(E_f)}{\sin\phi}] t'' 1$

$$\frac{dI_J}{dt} = \frac{\varepsilon \Delta \Omega \mu_\chi}{4\pi} e^{-\left(\frac{\mu_{tot}(E)}{\sin\theta} + \frac{\mu_{tot}(E_f)}{\sin\phi} \right) t} + \mu_\chi \approx \mu_\chi \tag{60}$$

This signal variation is heavily dependent on the transmitted signal, implying that when this is achieved, the effect of self-absorption associated with large particles and high energy in the luminescence mode is adequately mitigated.

The above two results are demonstrated in Fig. 15, showing that when the combined sorting scheme is used and that by implementing the signal I_J defined by (58), the derived signals of a joined luminescence and transmission modes are distinctly defined by lines which are parallel to each other. This removes the possibility of any two-lines crossing each other, which would result in poor classification. Notice that when the two lines cross $I_i = I_j$ or $I_i/I_j = 1$, which is just a statement of poor inter-signal contrast.

Tables 1 and 2. Show contrast poor in the XRL signal at thin sample while the is good contrast after joining the two modes.
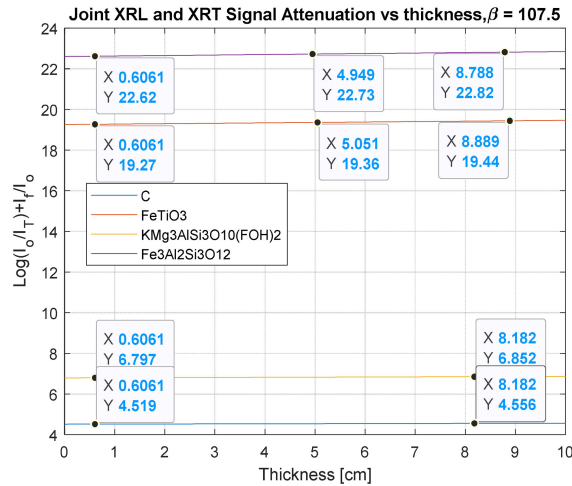
Fig 15. Combined Monochromatic XRL and XRT Diamond Sorter.

TABLE 2

Monochromatic Contrast Performance Post-System Joining.

Contrast	XRT	
	$< 10mm$	$> 32mm$
I_o/I_c (dB)	3.55	3.55

4.2 Polychromatic Sorting: Exafs Sorting Model

The polychromatic XRL analytical model is based on the luminescence EXAFS signal. Eqn. (27) is a summation of all atomic species around the absorbing atom, without loss of generality, two atomic species is considered for ease of mathematics. This approach is justified as succeeding mathematical manipulations are themselves distributive and linear. Thus, for the two-atom species, a compact luminescence EXAFS signal is;

$$\chi_{L12}(k) = [A_1(k)\sin(2kr_1 + \delta_1(k)) + A_2(k)\sin(2kr_2 + \delta_2(k))] * f(E) \tag{61}$$

Where $f(E)$ is our self-absorption model and $A_1(k)$ and $A_2(k)$ are each defined by the amplitude of (4) for the different atomic species. To proceed, we need to transform $f(E)$ into the k space, which is defined by

$$f(E) \overset{k\ space}{\rightarrow} f\left(\frac{\bar{h}}{2m_e}\left(k^2 + k_0{}^2\right)\right) = \frac{\bar{h}}{2m_e}e^{-\gamma k_0{}^2}e^{-\gamma k^2} \tag{62}$$

It is important to understand the variation μ_L at low and high energies, and to simplify the derivative, we define:

$$\chi_{L12}(k) = [A_1(k)\sin(2kr_1 + \delta_1(k)) + A_2(k)\sin(2kr_2 + \delta_2(k))]\frac{\bar{h}}{2m_e}e^{-\gamma k_0{}^2}e^{-\gamma k^2} \tag{63}$$

$$\lim_{k-Large}\chi_{L12}(k) = 0 , \tag{64}$$

signifying that the EXAFS luminescence sinusoid is annihilated at high energies, leading to loss of information. This phenomenon is self-absorption associated with the EXAFS luminescence signal. See the results in Fig. 16.

While

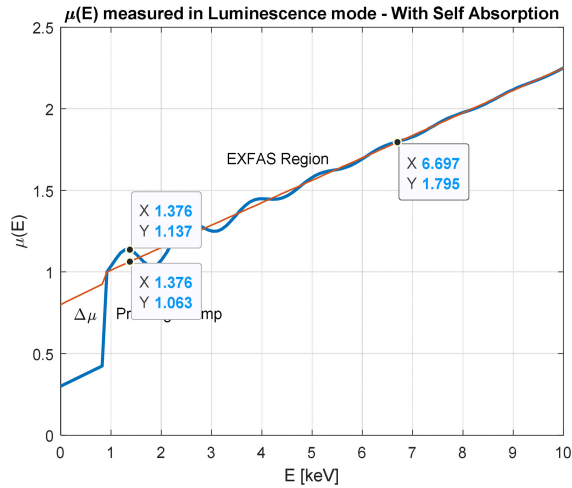$$\lim_{k\rightarrow small/medium}\chi_{L12}(k) \neq 0 \tag{65}$$

Fig. 16. Absorption Coefficient in Luminescence affected by Self-Absorption.
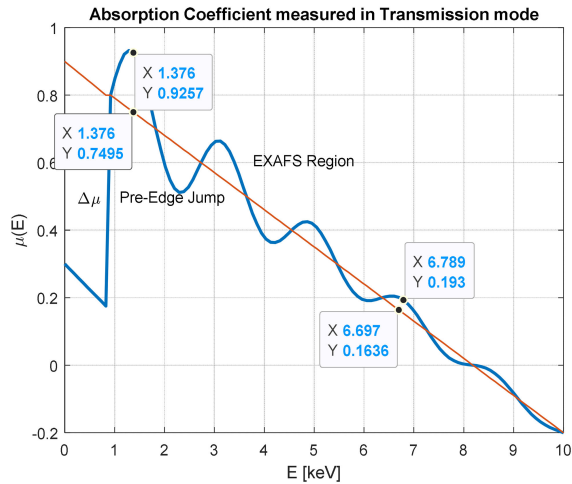

Fig. 17. Absorption Coefficient in Transmission not affected by Self-Absorption.

4.2.1 Polychromatic Xrt Analytical Model: The polychromatic XRT analytical model is based on the transmission EXAFS signal is:

$$\chi_{T12}(k) = [A_1(k)\sin(2kr_1 + \delta_1(k)) + A_2(k)\sin(2kr_2 + \delta_2(k))] \tag{66}$$

And

$$\lim_{k-Large} \chi_{T12}(k) \neq 0 \tag{67}$$

The exponential term outside the bracket in (63) is not present in (66), as XRT- EXAFS is immune to the self-absorption effect, and hence high energy sinusoids persist to exist. This is an XRT system strength as it is able to retain information at high energies, Fig. 17.

It is important to note that both $A_1(k)$ and $A_2(k)$ do have a $e^{-2k^2\sigma^2}$ dependence due to the Debye-Waller factor. However, in the case of XRL another factor $e^{-\gamma k^2}$, makes the signal attenuation more aggressive, the context of (66) is not entirely true, but true in relative terms, the XRL signal is fast decaying because of the self-absorption factor, and in the energy region of interest the XRT signal preserves the sinusoidal information, while it is a known fact that in the limit of very high k, or E, the XRT signal will be attenuated by the Debye-Waller factor present in both modes.
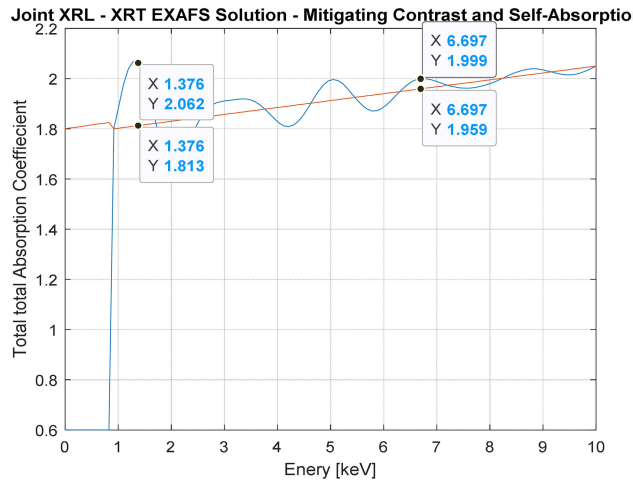
Fig. 18. Combined EXAFS XRL and XRT Absorption Coefficient.

TABLE 3

Polychromatic Self-Absorption Performance Pre-System Joining.

Self-absorption	XRT		XRL	
(*variation of sinusoid from asymptote at high energy*)	*at 60keV*	*at 80keV*	*at 60keV*	*at 80keV*
	25 %	68%	0%	0%

TABLE 4

Polychromatic Self-Absorption Performance Post System Joining

Self-absorption	XRL/XRT		This signal preservation allows for a k^2 weighting of the resultant combined signal for full signal recovery.
(*variation of sinusoid from asymptote at high energy*)	*at 60keV*	*at 80keV*	
	5%	6%	

4.2.2 Combined Polychromatic Sorting Model: Given the strengths and weaknesses of each model, a model consisting of both XRL and XRT EXAFS signal simultaneously will clearly mitigate the weaknesses of each system. The combined EXAFS signal is:

$$\chi_{L12} + \chi_{T12} = [A_1(k)\sin(2kr_1 + \delta_1(k)) + A_2(k)\sin(2kr_2 + \delta_2(k))] \frac{\bar{h}}{2m_e} e^{-\gamma k_0^2} e^{-\gamma k^2}$$

$$+ [A_1(k)\sin(2kr_1 + \delta_1(k)) + A_2(k)\sin(2kr_2 + \delta_2(k))] \quad (68)$$

By combining the derivatives of χ_{L12} and χ_{T12} is clear that:

$$\lim_{k \to large} \chi_{L12} + \chi_{T12} \neq 0 \quad (69)$$

so that the EXAFS signal, especially the sinusoid variation, is preserved, eliminating the effect of self-absorption through incorporating the XRT signal, Fig. 18.

Self-absorption is demonstrated in Tables 3 and 4 for the single mode XRL signal. The pre-joining table show that there is no preservation of the XRL signal at high energies while there is good signal preservation in the XRT mode. The post joining table show that when the two system are combined there is signal preservation in the total signal.
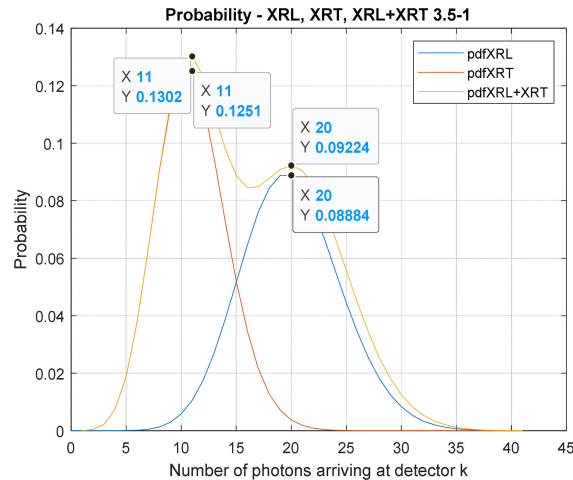
Fig 19. Pdf XRL, Pdf XRT, and Combined Pdf.

5. Detectability Improvement

Fig. 17 shows that a combined system leads to good detectability. A close analytical way of modeling this is to consider the arrival of photons at each detector, XRL or XRT, as a Poisson process and show that when the two systems are joined, there is a good chance of improving detection.

Let L to be an XRL event defined by N_L as the average number of photons arriving at the detector in time interval Δt, which can be seconds, milliseconds, or any desired time interval, resulting in a current I_L. Further, let T to be an XRT event defined by N_T as the average number of photons arriving at the detector in the same time interval, resulting in a current I_T. The probability that a current I_L or I_T produced at the detector, due to k photons arriving at the detector is:

$$P_L(k, N_L) = \frac{N_L{}^k e^{-N_L}}{k!} \tag{70}$$

While

$$P_T(k, N_T) = \frac{N_T{}^k e^{-N_T}}{k!} \tag{71}$$

Because the events L and T are independent and identically distributed [51], one can determine the probability of a combined event $L \cup T$, analogous to the addition of the signals from the XRL sensor and XRT sensor.

$$P(LUT) = P_L(k, N_L) + P_T(k, N_T) - P_L(k, N_L) P_T(k, N_T) = \frac{N_L{}^k e^{-N_L}}{k!} + \frac{N_T{}^k e^{-N_T}}{k!} - \frac{N_L{}^k e^{-N_L}}{k!} \frac{N_T{}^k e^{-N_T}}{k!} \tag{72}$$

A detection rate comparison is made, Fig. 19, by selecting some arbitrary averages $N_L = 20$ and $N_T = 10$, for $k = 1\ldots.40$, the probability distribution function P_L, P_T and $P(LUT)$. The area under each pdf, is the probability of detection for each mode and the area under $P(LUT)$ is greater than the areas under P_T and P_L respectively. Meaning that the combined model offers better chances of classifying materials correctly than when single modes are used.

5.1 Proposed Dual Modality Sorting Design

Fig. 20 is the machine design as informed by our joint analytical model, consisting of simultaneous measurement of the luminescence and transmission signals which are processed together in accordance with our joining schemes defined in monochromatic mode and polychromatic mode, respectively.
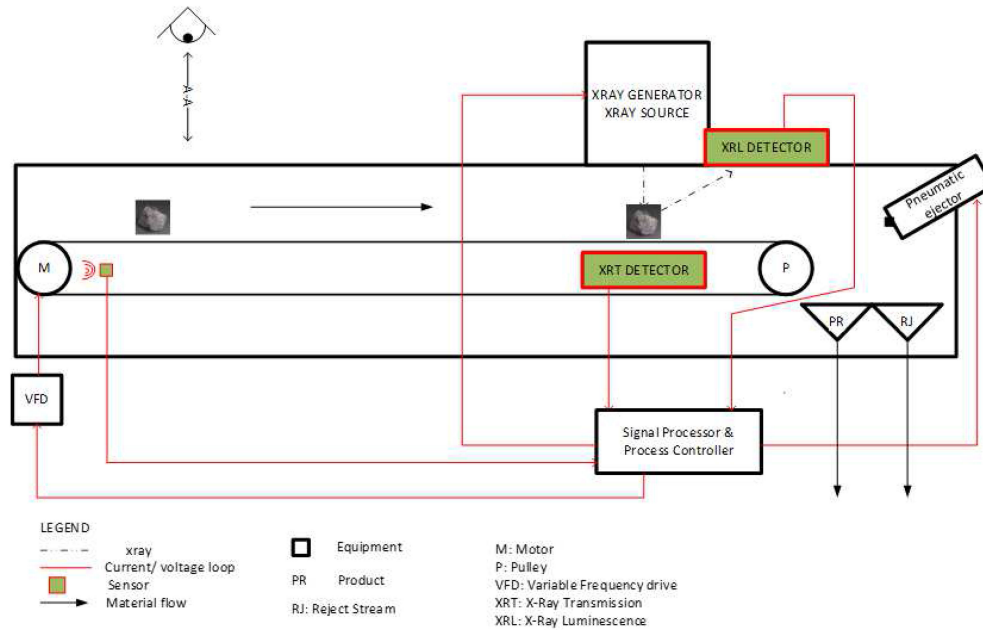
Fig. 20. Dual Mode Sorting Machine Model.

Luminescence/Fluorescence and transmission characterization rely on material absorption co-efficient. XRT measurements are immune to self-absorption (for large samples or at high energy) while they suffer poor contrast at small particles size, below 10mm. At the same time, XRL provides a more consistent contrast at all particle size ranges. In contrast, it suffers self-absorption and an approach that uses these signals simultaneously is useful both in the monochromatic case and in polychromatic case. The exact combined signals are as in eqn. (58) or,

$$
NR\left(\ln\left(\frac{I_t}{I_0}\right) + \beta\frac{I_f}{I_0} - \mu_\chi(E)t - \beta\frac{\varepsilon\Delta\Omega\mu_\chi(E)}{4\pi} \frac{\left\{1 - \left\{e^{-\left[\frac{\mu_\chi(E)+\mu_{other}(E)}{\sin\theta} + \frac{\mu_\chi(E_f)+\mu_{other}(E_f)}{\sin\phi}\right]t}\right\}\right\}}{\left[\frac{\mu_\chi(E)+\mu_{other}(E)}{\sin\theta} + \frac{\mu_\chi(E_f)+\mu_{other}(E_f)}{\sin\phi}\right]} = 0, \mu_\chi(E), \tau\right)
$$

(73)

Where $NR(f, x, \tau)$ is a Newton Raphson algorithm that solves the equation $f(x) = 0$, truncating the iterations when the tolerance τ is attained and I_t and I_f are measured intensities at the transmission and fluorescence detectors, and I_0, E, E_f are the intensity of the incident photoelectrons, E is the energy of the incident photoelectrons and E_f is the energy of the fluorescence photoelectrons, with μ in eqn. (10) and (11) divided into its constituents $\mu_\chi(E)$ for the target material and $\mu_{other}(E)$ for the other material. Our objective is to solve for $\mu_\chi(E)$. This approach can be considered monochromatic or polychromatic, depending on the user's choice of simulation. The solution of eqn. (73) is a numerical approximation of eqn. (28) but with effects XRL and XRT measurements infused in the final signal.

Formally our analytical solution at the $n + 1th$ iteration is given by,

$$
\mu_{\chi,n+1} = \mu_{\chi,n} - \frac{f\left(\mu_{\chi,n}\right)}{f'\left(\mu_{\chi,n}\right)}
$$

(74)

By defining a new function

$$
f\left(\mu_\chi\right) = I_t\left(\mu_\chi\right) + \beta I_f\left(\mu_\chi\right),
$$

(75)

then the absorption coefficient at the $n + 1$ iteration of the NR algorithm is given by.

$$\mu_{\chi,n+1} = \mu_{\chi,n} - \frac{l_t\left(\mu_{\chi,n}\right) + \beta l_f\left(\mu_{\chi,n}\right)}{l_t'\left(\mu_{\chi,n}\right) + \beta l_f'\left(\mu_{\chi,n}\right)} \tag{76}$$

It is clearly giving a final absorption coefficient that has inherited the advantages of both fluorescence and transmission measurements. Where β is a constant whose effect is to level the fluorescence energy to same scale as transmission scale or vice-versa. In terms of classification, it is perfectly legitimate to define a new function so long as a result is unique, which is the case with eqn. (75) since the functions l_t and l_f are unique functions of μ_χ.

6. Conclusion

We have shown in the present article, the review of literature of both X-ray transmission and X-ray luminescence methods of characterization in general and borrowed the concepts to develop a combined analytical model for X-ray luminescence and X-ray transmission sorting of diamonds. Critical factors to be considered during the model development were the limitations of each approach in elemental recovery or classification. We used two important metrics for evaluation to guide model developments, which demonstrate contrast improvement and self-absorption rejection. We considered Two extremes through the analysis. These were thin sample limitations and thick sample limitations. The important class of material and conditions that were also studied were the thick sample with $\mu_x \sim \mu_{other}$ or $\mu_x \sim \mu_{tot}$, providing a case for which it is very difficult to deal with self-absorption case typical in luminescence mode. A study of contrast enhancers and self-absorption rejection was done for both single energy source and polychromatic source. In the monochromatic state, it was clear that the transmission mode suffered poor contrast at a small particle size range, typically between $1 - 8.730mm$. The inclusion of a second data modality, luminescence, provides a good remedy against poor contrast associated with XRT signals at a small size range. The present findings described elsewhere in this article, helped concludes as follows: to deal with contrast for small size ranges, the combined addition of the XRT and XRL signal provides a perfect solution. Additionally, by observing that the luminescence mode which suffers from poor contrast in the large sample range (as a result of the self-absorption nature of large particles), the inclusion of the XRT signal to the XRL signal facilitates for self-absorption rejection that would be present in measurements taken in luminescence mode. This leads to another conclusion that the combined approach is perfect for managing self-absorption at large particle size range.

As for the monochromatic operating mode, the first approach can distinguish material through the use of the total absorption coefficient, and that is, as far as the information is concerned, one can gain information about the material in the first place. In doing so, a much better approach in so far as elemental identification is concerned is that the use of the EXAFS signal that contains various information ranging from atomic disorders, coordination numbers, atomic radii, and phase. This method relies on obtaining a set of absorption coefficient from a sample by pulsing the sample at high speed with X-ray energy from $6keV - 80\,keV$. We have also provided a simple model of the XRL-EXAFS signal, which we derived by incorporating our self-absorption model. This was compared with the XRT-EXAFS signal, and it was concluded that the XRL signal is aggressively attenuated at high energies. In contrast, the XRT-EXAFS signal preserves the sinusoid variations. The two models provide a good reference to understand, especially the phenomena of self-absorption experienced in luminescence. Thus, an implementation of sorting criteria that is solely based on luminescence will be futile for large samples at high energy settings. The inclusion of the XRT-EXAFS signal is an obvious remedy for this problem.

New futuristic applications are envisioned by employing the combined XRL and XRT sorting mode.

Acknowledgment

References

[1] H. Harbeck, and H. Kroog, "New developments in sensor-based sorting," *Mineral Process.*, vol. 49, no. 5, pp. 4–11, 2008.

[2] Marketwatch.com, "Synthetic diamond market size 2020 - Growth Opportunities and trends, industry drivers, business plans with share, competitors analysis, and global revenue forecast to 2024," Accessed: July 30, 2020. [Online]. Available: https://www.marketwatch.com/press-release/synthetic-diamond-market-size-2020---growth-opportunities-and-trends-industry-drivers-business-plans-with-share-competitors-analysis-and-global-revenue-forecast-to-2024-2020-10-01

[3] N. Rötzer, and M. Schmidt, "Decreasing metal ore grades—Is the fear of resource depletion justified?," *Resources*, vol. 7, no. 88, pp. 1–14, 2018.

[4] R. Knut, and O. Karis, "Spectroscopic investigations of electronic structure," *Sci. Technol. At., Mol., Condens. Matter Biol. Syst. Adv. Funct. Mater.*, vol. 2, pp. 45–70, 2012.

[5] F. Riedel, and M. Dehler, "Recovery of unliberated diamonds by X-ray transmission sorting," *J. Southern Afr. Inst. Mining Metall.*, vol. 110, pp. 193–199, 2010.

[6] J. Muralidhar, U. Patnaik, S. Misra, and Rajeev, "Extraction and rapid X-ray fluorescence spectrometric determination of tungsten in ore-dressing products of scheelite," *X-Ray Spectrometry*, vol. 27, pp. 117–120, 1998.

[7] X-Ray Mass Attenuation Coefficients, National Institute of Standards and Technology, 2020. Accessed: July 30, 2020. [Online]. Available: https://physics.nist.gov/PhysRefData/XrayMassCoef/tab1.html

[8] E. G. D. Santos, R. S. Paranhos, C. O. Petter, A. Young, and M. M. Veras, "Preliminary analysis of the application of sensor based sorting on a limestone mine in the region caçapava do sul, Brazil," *Proc. 3rd Pan Amer. Mater. Congr. Minerals Met. Mater. Ser.*, pp. 579–586, 2017.

[9] S. Huang *et al.*, "Modeling and quantitative analysis of X-ray transmission and backscatter imaging aimed at security inspection," *Opt. Exp.*, vol. 27, no. 2, pp. 337–349, 2019.

[10] C. H. Booth, and F. Bridges, "Improved self-absorption correction for fluorescence measurements of extended X-Ray absorption fine-structure," *Physica Scripta*, vol. T115, pp. 202–204, 2005.

[11] R. M. Trevorah, C. T. Chantler, and M. J. Schalken, "Solving self-absorption in fluorescence," *IUCrJ*, vol. 6, pp. 586–602, 2019.

[12] P. Pfalzer *et al.*, "Elimination of self-absorption in fluorescence hard-X-ray absorption spectra," *Phys. Rev. B*, vol. 60, pp. 9335–9339, 1999.

[13] L. Tröger *et al.*, "Full correction of the self-absorption in soft-fluorescence extended X-ray-absorption fine structure," *Phys. Rev. B*, vol. 46, pp. 3283–3289, 1992.

[14] A. Alter, "Physical principles of medical imaging by perry sprawls," *Jr. Med. Phys.*, vol. 15, pp. 274–274, 1988.

[15] R. Knut, and O. Karis, "Spectroscopic investigations of electronic structure," *Sci. Technol. At., Mol., Condens. Matter Biol. Syst. Adv. Funct. Mater.*, vol. 2, pp. 45–70, 2012.

[16] A. Gaur, and B. D. Shrivastava, "Speciation using X-Ray absorption fine structure (XAFS)," *Rev. J. Chem.*, vol. 5, no. 4, pp. 361–398, 2015.

[17] EXAFS: Extended X-ray Absorption Fine Structure -Diamond Light Source. Diamond.ac.uk 2020. [Online]. Available: https://www.diamond.ac.uk/Instruments/Techniques/Spectroscopy/EXAFS.html

[18] F. Riedel, and M. Dehler, "Recovery of unliberated diamonds by X-ray transmission sorting," *J. Southern Afr. Inst. Mining Metall.*, vol. 110, pp. 193–199, 2010.

[19] P. Van der Westhuyzen, and A. Jakins, "Current trends in the development of new or optimization of existing diamond processing plants, with focus on beneficiation," *J. Southern Afr. Inst. Mining Metall.*, vol. 114, pp. 537–546, 2014.

[20] J. Danoczi, and A. Koursaris, "Development of luminescent diamond simulants for X-ray recovery," *J. Southern Afr. Inst. Mining Metall.*, vol. 108, pp. 89–97, 2008.

[21] R. H. Mitchell, "Kimberlites and lamproites: Primary sources of diamond," *Geosci. Canada*, vol. 18, no. 1, pp. 1–6, Mar. 1991.

[22] A. Anupam, S. Bhattacharya, and G. de Korte, "Effect of feed size and size distribution on the performance of dense medium cyclones: A critical review," *Int. J. Coal Preparation Utilization*, vol. 40, no. 9, pp. 618–639, 2020.

[23] H. Zughbi, M. Schwarz, W. Turner, and W. Hutton, "Numerical and experimental investigations of wear in heavy medium cyclones," *Minerals Eng.*, vol. 4, pp. 245–262, 1991.

[24] National Institute of Standards and Technology "*X-Ray Mass Attenuation Coefficients*," 2020. Accessed: July 30, 2020. [Online]. Available: https://physics.nist.gov/PhysRefData/XrayMassCoef/tab1.html

[25] B. Akça, and S. Erzeneoğlu, "The mass attenuation coefficients, electronic, atomic, and molecular cross sections, effective atomic numbers, and electron densities for compounds of some biomedically important elements at 59.5 keV," *Sci. Technol. Nucl. Installations*, pp. 1–8, 2014.

[26] T. Jensen, and J. Gray, "Monochromatic x-ray beams for NDT," In: Review of progress in quantitative nondestructive evaluation. *Proc. 18th Ann. Review*, Brunswick, ME (United States), July 28-Aug. 2, 1991, vol. 11A, pp. 339–345, 1991.

[27] F. Meirer *et al.*, "Parameter study of self-absorption effects in total reflection X-ray Fluorescence–X-ray absorption near edge structure analysis of arsenic," *Spectrochimica Acta Part B: At. Spectrosc.*, vol. 63, pp. 1496–1502, 2008.

[28] E.I. Erlich, W. Dan Hausel, "Diamond deposits," *Soc. for Mining, Metall. Exploration*, vol. 1, pp. 74–94, 2002.

[29] X. Castañer, and C. Prieto, "Fluorescence detection of extended X-Ray absorption fine structure in thin films," *J. de Physique III, EDP Sci.*, vol. 7, no. 2, pp. 337–349, 1997.

[30] M. R. Robben, H. Knapp, M. Dehler, and H. Wortruba, "X-ray transmission of sorting tungsten ore," *Opt. Characterization Mater.*, pp. 245–258, 2013.

[31] W. D. Hausel, "Diamonds in Industrial Minerals and Rocks," *Soc. for Mining, Metall. Exploration*, vol. 7, pp. 415–433, 2006.

[32] Z. Tan, J. Budnick, and S. Heald, "Structural parameter determination in fluorescence EXAFS of concentrated samples," *Rev. Sci. Instruments*, vol. 60, pp. 1021–1025, 1989.

[33] D. Spencer, "The high-speed identification and sorting of nonferrous scrap," *JOM*, vol. 57, pp. 46–51, 2005.

[34] F. Alcalde Bessia *et al.*, "X-ray micrographic imaging system based on COTS CMOS sensors," *Int. J. Circuit Theory Appl.*, vol. 46, pp. 1848–1857, 2018.

[35] C. Kleine, M. Robben, and H. Wotruba "Theory and operational experience of X-ray transmission sorting in the minerals industry," in *Proc. Phys. Sepamtio*, Falmouth, U.K., pp. 411–424, 2011.

[36] K. Neubert, and H. Wotruba, "Investigations on the detectability of rare-earth minerals using dual-energy X-ray transmission sorting," *J. Sustain. Metall.*, vol. 3, pp. 3–12, 2016.

[37] P. Kleimann, J. Linnros, C. Frojdh, and C. Petersson, "An X-ray imaging pixel detector based on a scintillating guides screen," *IEEE Trans. Nuclear Sci.*, vol. 47, no. 4, pp. 1483–1486, Aug. 2000.

[38] J. Rocha, N. Ramos, S. Lanceros-Mendez, R. Wolffenbuttel, and J. Correia, "CMOS X-rays detector array based on scintillating light guides," *Sensors Actuators A: Phys.*, vol. 110, pp. 119–123, 2004.

[39] E. Dubaric, C. Fröjdh, H.-E. Nilsson, and C. Petersson, "Resolution and noise properties of scintillator coated X-ray detectors," *Nucl. Instruments Methods Phys. Res. Sect. A: Accelerators, Spectrometers, Detectors Assoc. Equip.*, vol. 466, pp. 178–182, 2001.

[40] E. Dubaric, C. Fröjdh, H.-E. Nilsson, and C. Petersson, "Resolution and noise properties of scintillator coated X-ray detectors," *Nucl. Instruments Methods Phys. Res. Sect. A: Accelerators, Spectrometers, Detectors Assoc. Equip.*, vol. 466, pp. 178–182, 2001.

[41] J. H. Hubbell, "Photon mass attenuation and mass energy-absorption coefficients for h, c, n, o, ar, and seven mixtures from 0.1 keV to 20 meV, "*Radiat. Res.*, vol. 70, pp. 58–81, 1977.

[42] M. Hjelm, B. Norlin, H.-E. Nilsson, C. Fröjdh, and X. Badel, "Monte Carlo simulation of the imaging properties of scintillator-coated X-ray pixel detectors," *Nucl. Instruments Methods Phys. Res. Sect. A: Accelerators, Spectrometers, Detectors and Assoc. Equip.* vol. 509, pp. 76–85, 2003.

[43] R. Dinapoli *et al.*, "EIGER: Next generation single photon counting detector for X-ray applications," *Nucl. Instruments Methods Phys. Res. Sect. A: Accelerators, Spectrometers, Detectors Assoc. Equip.*, vol. 650, pp. 79–83, 2011.